Vol. 16 • No. 40 • October 8 • 2020

www.small-journal.com

NANO · MICRO small

WILEY-VCH

NANO · MICRO small
www.small-journal.com

Sodiophilically Graded Gold Coating on Carbon Skeletons for Highly Stable Sodium Metal Anodes

Junxiong Wu, Peichao Zou, Muhammad Ihsan-Ul-Haq, Nauman Mubarak, Alessandro Susca, Baohua Li, Francesco Ciucci, and Jang-Kyo Kim**

Metallic sodium (Na) is an appealing anode material for high-energy Na batteries. However, Na metal suffers from low coulombic efficiencies and severe dendrite growth during plating/stripping cycles, causing short circuits. As an effective strategy to improve the deposition behavior of Na metal, a 3D carbon foam is developed that is sputter-coated with gold nanoparticles (Au/CF), forming a functional gradient through its thickness. The highly porous Au/CF host is proven to have gradually varying sodiophilicity, which in turn facilitates initially preferential Na deposition on the gold-rich, sodiophilic region in a "bottom-up growth" mode, leading to uniform plating over the entire Au/CF host. This finding contrasts with dendrite formation in the pristine CF host, as proven by in situ microscopy. The Na-predeposited Au/CF (Na@Au/CF) composite anode operates steadily for 1000 h at a low overpotential of ≈20 mV at 2 mA cm^{-2} in a symmetric cell. When the composite anode is coupled with a $Na_3V_2(PO_4)_2F_3$ cathode, the full cell has a high capacity of 102.1 mAh g^{-1} after 500 cycles at 2 C. The sodiophilicity gradient design that is explored in this study offers new insight into developing porous Na metal hosts with highly stable plating/stripping performance for next-generation Na batteries.

1. Introduction

High-energy electrochemical energy storage devices are attracting increasing attention owing to the ever-growing demand in portable electronics, electric cars, and grid storage systems.[1–5] Sodium (Na) metal is recognized as an attractive anode material for Na batteries because of its high theoretical specific capacity of 1166 mAh g^{-1} and low electrochemical potential of −2.714 V versus the standard hydrogen electrode.[4,6,7] However, Na-metal batteries (NMBs) have several challenges due to the presence of metallic Na, including, 1) the non-uniform deposition of Na which leads to the uncontrollable growth of Na dendrite, eventually short-circuiting the batteries, 2) the large volume changes occurring during plating/stripping cycles because of its hostless nature, and 3) the formation of unstable solid electrolyte interphase (SEI) layers at the expense of continuous depletion of the electrolyte.[3,7,8] In fact, all these issues are interrelated and lower the coulombic efficiency (CE), trigger serious safety hazards, and are ultimately responsible for the short lifespan of NMBs.[7,9,10]

Many efforts have been directed to circumventing these challenges, including the optimization of electrolyte composition,[11–13] the construction of artificial SEI layers,[14–16] the modulation of morphology/structure of current collectors and hosts,[17–24] the building of interlayers,[10,25] and the use of solid-state electrolytes.[26,27] Among these options, plating Na metal in 3D hosts is an effective approach not only to accommodate the large volume change of Na metal during plating and stripping but also to reduce the local current densities, thus mitigating the Na dendrite growth and reversibility issues.[17–23,28] Owing to these benefits, 3D skeletons prepared using graphene,[21] MXene,[29] freestanding carbonaceous materials,[18,19,23] and porous metal current collectors[17,20,28] have emerged as popular hosts for Na metal anodes. Nevertheless, their inherently low Na affinity makes these materials susceptible to suboptimal nucleation and growth of Na metal.[17,23,30] To prevent this issue, sodiophilic seeds or functional groups have been introduced into these 3D hosts. Sodiophilic nucleation sites, including metals (Mg,[31] Ag,[32,33] Au,[34] and Sn[35]) and metal

Dr. J. Wu, Dr. M. Ihsan-Ul-Haq, N. Mubarak, A. Susca, Prof. F. Ciucci, Prof. J.-K. Kim
Department of Mechanical and Aerospace Engineering
The Hong Kong University of Science and Technology
Clear Water Bay, Kowloon, Hong Kong, China
E-mail: francesco.ciucci@ust.hk; mejkkim@ust.hk
Dr. P. Zou
Department of Physics and Astronomy
University of California Irvine
Irvine CA92697, USA
Prof. B. Li
Shenzhen Key Laboratory on Power Battery Safety and Shenzhen Geim Graphene Center
Tsinghua Shenzhen International Graduate School
Tsinghua University
Guangdong 518055, China
Prof. F. Ciucci
Department of Chemical and Biological Engineering
The Hong Kong University of Science and Technology
Clear Water Bay, Hong Kong, China
The ORCID identification number(s) for the author(s) of this article can be found under https://doi.org/10.1002/smll.202003815.

DOI: 10.1002/smll.202003815

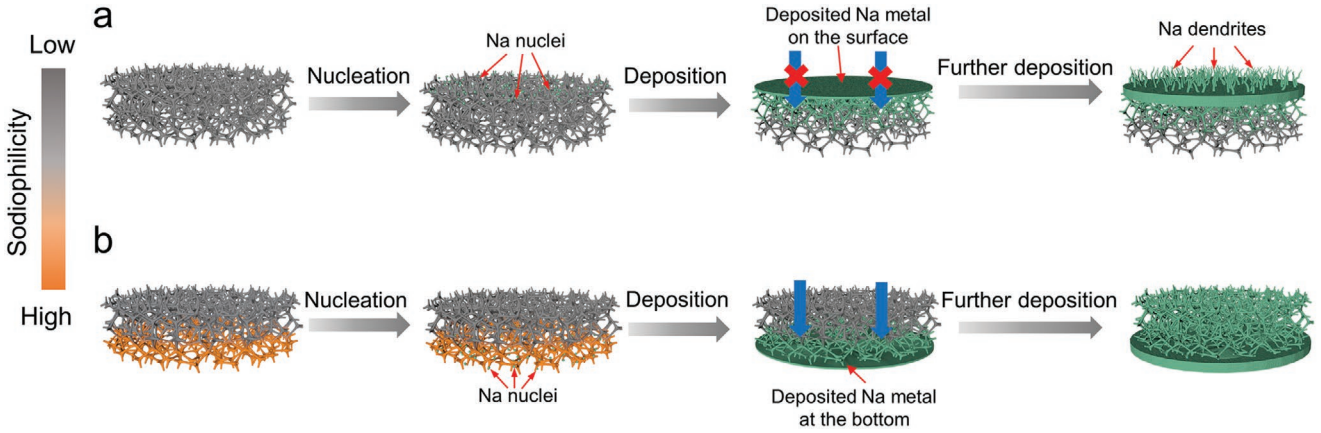

Figure 1. Schematic diagrams of Na nucleation and growth in the a) carbon foam without Au coating and b) sodiophilically graded carbon foam with Au coating.

oxides (Fe_2O_3[36] and SnO_2[37]), have been extensively explored for stable Na plating/stripping. Sodiophilic functional groups have also been introduced to guide the growth of Na metal. For example, carbon nanotubes have been functionalized with oxygen groups by microwave oxygen plasma.[38] This treatment lowered the overpotential of Na nucleation and mediated the subsequent Na growth without dendrite formation.

It has been experimentally and theoretically reported that Li plating initiates on the top surface of a 3D conductive scaffold, this is commonly called "top-growth" mode, because of the higher Li-ion concentration and lower transport resistances associated with that location.[39] To resolve the issues of locally concentrated deposition and Li dendrite growth, several strategies were successfully introduced, such as conductivity/lithiophilicity gradient hosts, lithiophilic-lithiophobic hosts, and interfacial layers.[39–41] Here, such a functionally-graded approach is explored for the first time to design the Na metal host for addressing the eccentric Na deposition behavior in NMBs. A schematic diagram shown in **Figure 1**a presents how the local accumulation of Na metal occurs on the top surface of a porous carbon scaffold. The local Na buildup not only generates a significant volume expansion in the electrode but also blocks the diffusion of Na-ion into its lower part. Therefore, the internal section of the 3D porous hosts is poorly utilized. In addition, as the initial Na plating is not homogeneous on the surface, the subsequent deposition will preferentially occur on the defects such as humps, finally resulting in Na dendrites or dead Na. In contrast, selectively applying the sodiophilic materials to the bottom of 3D structured anodes can promote the Na growth at the bottom instead of on the top surface, as schematically shown in Figure 1b, reducing the probability of unsafe dendrite formation on the top surface and accommodating the Na in the skeleton.

Here, we report a novel Na metal host (Au/CF) with a sodiophilicity gradient through the thickness of a 3D CF by sputtering Au nanoparticles on its bottom part. CF was chosen as the 3D host because of its high porosity, lightweight, and excellent electronic conductivity. Unlike the "top-growth" Na deposition on the pristine CF electrode, the sodiophilically graded Au/CF host facilitated the "bottom-up growth" of Na toward the top surface. As a result, the Au/CF host displayed a high CE of 99.5% for 300 h with a plating capacity of 1 mAh cm^{-2} at 1 mA cm^{-2}, while the CEs maintained high levels even after the capacity increased to 10 mAh cm^{-2}. In symmetric cells, the Na-predeposited Au/CF (Na@Au/CF) anodes operated steadily for 1000 h at 2 mA cm^{-2}. Also, when the composite anodes were coupled with $Na_3V_2(PO_4)_2F_3$ (NVPF) and sulfurized polyacrylonitrile (SPAN) cathodes, the full cells exhibited much better electrochemical performance than the cells prepared using the Na@CF anodes.

2. Results and Discussion

2.1. Fabrication and Characterization of Au/CF Electrode

Figure 2a illustrates the fabrication procedure of the Au/CF electrode. The commercial melamine foam was first carbonized at 1000 °C for 2 h under N_2 flow to form CF. Au nanoparticles were injected from the bottom side of the CF by magnetron sputtering. Because of the open pores and interconnected internal space in the CF, it was possible to create the Au coating with a gradually diminishing concentration from the backside toward the front surface of the CF, as discussed below. Therefore, the inset images reveal that the Au-rich bottom surface of the Au/CF is yellow, while the Au-deficient top side is black. The melamine foam had an innately interconnected porous structure (Figure S1a, Supporting Information), and the CF retained the 3D architecture after carbonization (Figure S1b, Supporting Information). Even after Au modification, the porous structure was maintained intact (Figure 2b). The X-ray diffraction (XRD) patterns of CF and Au/CF shown in Figure 2c confirm the successful Au coating. The broad peak at ≈25° corresponds to amorphous carbon, while the distinct peaks at 38.3°, 44.5°, 64.7°, and 77.7° are assigned to the (111), (200), (220), and (311) planes of Au, respectively. The transmission electron microscopy image and elemental maps in Figure S2, Supporting Information, manifest homogeneously coated, ultrafine Au nanoparticles on the CF surface. The Au nanoparticles were of 5–10 nm in diameter and had a lattice spacing of ≈0.235 nm corresponding to the (111) plane of Au (Figure 2d).[42] The selected area electron diffraction (SAED) pattern (inset of Figure 2d) presents the diffraction rings of Au nanocrystal, agreeing with the XRD results.

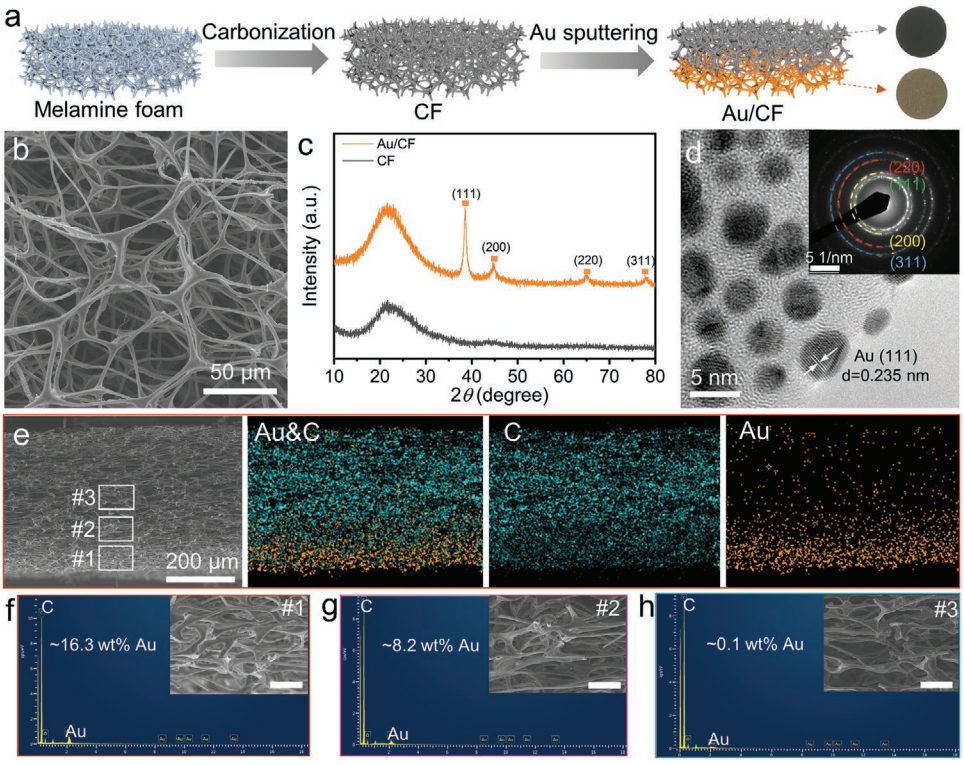

Figure 2. Preparation and characterization of Au/CF host. a) Schematic illustration of the fabrication process of the Au/CF host with the inset showing the digital images of the top and bottom surfaces. b) SEM image of Au/CF, c) XRD patterns of CF and Au/CF, d) HRTEM image of Au/CF with SAED patterns in the inset. e) Cross-sectional SEM images of Au/CF with the corresponding EDX maps. f–h) EDX spectrograms of the lower (region #1), middle (region #2), and upper (region #3) parts marked in (e), respectively. The scale bar in insets of (f–h) is 20 μm.

The Au distribution in the Au/CF host was further characterized by scanning electron microscopy (SEM) and elemental maps. The average thickness of the Au/CF was ≈400 μm, and the Au coating was abundant on the back surface, with its concentration diminishing toward the front surface (Figure 2e). The gradual change in Au concentration led to the formation of a functionally-graded structure with a higher Au concentration corresponding to higher sodiophilicity at the back surface and vice versa. Furthermore, the Au content was measured across the Au/CF thickness using energy-dispersive X-ray (EDX) spectrograms and elemental maps (Figure 2f–h and Figure S3, Supporting Information). The lower, middle, and upper parts, indicated by region #1, #2, and #3, presented a similarly porous morphology, with largely varying Au contents of ≈16.3, ≈8.2, and ≈0.1 wt%, respectively, demonstrating the success of the Au gradient in the Au/CF host. Figure S4, Supporting Information, shows the SEM images and EDX spectrograms of the top and bottom surfaces, further confirming the even distribution of the Au nanoparticles on the bottom surface and no Au coating on the front. The X-ray photoelectron spectra (XPS) were recorded from the bottom surfaces of the Au/CF and CF, as shown in Figure S5, Supporting Information. Both the survey and Au 4f spectra of Au/CF exhibit distinct Au peaks while no such peaks are observed from the CF surface, in agreement with the EDX results. In addition, the porosity and electronic conductivity of the CF before and after Au coating are compared. The results show that the Au coating had a negligible effect on porosity but significantly increased the electronic conductivity from 50.4 to 150.7 S m^{-1}, to the advantage of electrode performance in NMBs.

2.2. Deposition Behavior of Na in Au/CF Electrode

Before delving into the Na deposition behavior, the electrolyte wettability of Au/CF and CF was evaluated by measuring the contact angles. The contact angles of electrolyte droplets applied onto the surface of the CF and Au/CF electrodes are shown in Figure S6, Supporting Information. The former had an initial contact angle of ≈15°, and the value for the latter is ≈19°, implying that the electrolyte wetted both surfaces, thereby ensuring fast Na ion transportation and low concentration polarization. To investigate the Na deposition behavior, half-cells were assembled with Na metal as the counter electrode, as shown in Figure S7a, Supporting Information. The plating amount of Na was controlled to 2 and 4 mAh cm^{-2} at an areal current of 0.5 mA cm^{-2}. **Figure 3** presents a significantly different Na plating performance between the two types of electrodes. Na was deposited preferentially on the top surface of CF, while the bottom region remained porous with sparsely filled Na (Figure 3a–c). This observation can be attributed to the short pathways for Na ions to accept the electrons at the anode/separator interface.[39,41] Unlike the CF electrode, however, the bottom region of the Au/CF electrode coated with Au nuclei was filled first with dense Na, while the top region started to fill later (Figure 3d–f). The "top-growth" and "bottom-up growth" modes in the CF and Au/CF hosts, respectively, are further demonstrated by the optical images shown in Figure S8, Supporting Information. To illustrate the spatial control of Na deposition and the efficient suppression of Na dendrite growth,

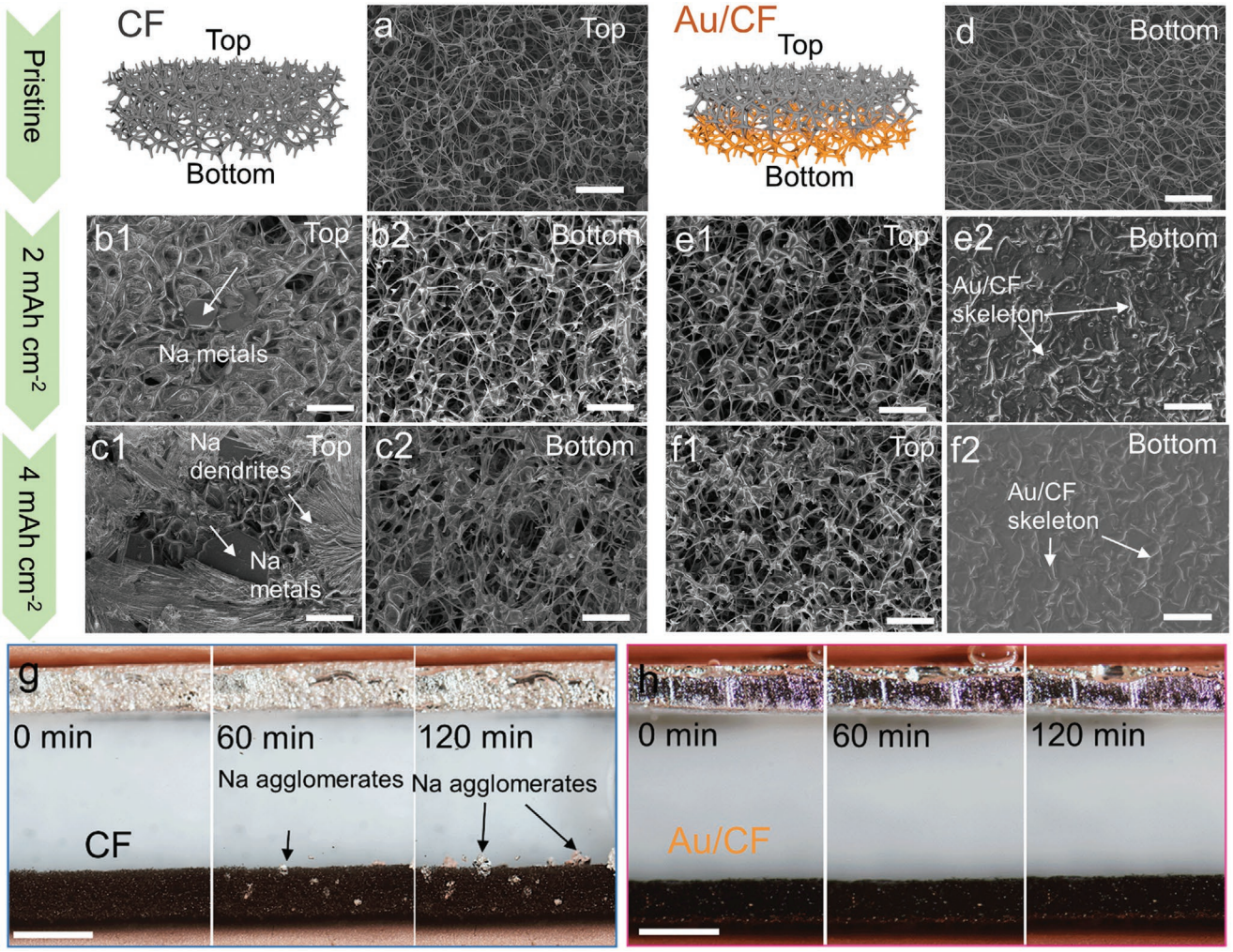

Figure 3. Deposition behavior of Na in the CF and Au/CF hosts at an areal current of 0.5 mA cm^{-2}. SEM images of the CF electrode surface morphologies before and after plating: a) pristine CF, b1,b2) after plating 2 mAh cm^{-2} Na, c1,c2) after plating 4 mAh cm^{-2} Na. SEM images of the Au/CF electrode surface before and after Na plating: d) Au/CF before plating, e1,e2) after plating 2 mAh cm^{-2} Na, f1,f2) after plating 4 mAh cm^{-2} Na. The scale bar in (a–f) is 100 µm. In situ optical photographs of Na deposition on g) CF and h) Au/CF captured by a digital camera. The current density is 0.5 mA cm^{-2} and the scale bar in (g,h) is 400 µm.

in situ optical microscope images were taken of the dynamic process of Na plating in real-time (Movies S1 and S2, Supporting Information). As shown in Figure 3g, Na dendrites started growing on the surface of the CF substrate, which became increasingly evident over time. Conversely, no obvious Na dendrites were found on the surface of the Au/CF electrode over the whole period of observation. The lack of dendrites may be attributed to the selective nucleation of Na ions in the interior skeleton of the Au/CF (Figure 3h).

The morphologies of the cycled electrodes were examined by SEM, and the evolution of morphologies are shown in Figure S9, Supporting Information. For the CF electrode, a mass of Na agglomerates was observed on the top surface after the 50th plating cycle at a Na capacity of 2 mAh cm^{-2} (Figure S9a, Supporting Information). Meanwhile, there was almost no Na on the bottom part of the CF electrode (Figure S9b, Supporting Information), again demonstrating preferential Na deposition on the top surface of CF. For the Au/CF electrode, there was almost no significant change between the first and the 50th plating cycles (Figure S9c,d). We also studied Na deposition on Au/CF at higher areal currents of 2 and 5 mA cm^{-2}. As shown in Figure S10a, Supporting Information, part of Na metal was deposited on the top surface of the electrode with the amount far less than that on the CF top surface (Figure S10b, Supporting Information). Besides, its bottom surface was filled with Na, unlike the CF electrode (Figure S10d,e, Supporting Information). When the areal current was increased to 5 mA cm^{-2}, the preferential deposition of Na at its bottom part became less prominent due to the increased overpotential, which promoted Na nucleation and growth (Figure S10c,f, Supporting Information).

To reveal the role of the Au nucleation sites, the Na affinity on different substrates was studied using the density functional theory (DFT). The formation energies of Na-Au binaries were first computed, as shown in **Figure 4**a. The convex hull of Na-Au binaries for different compositions indicates that $NaAu_2$

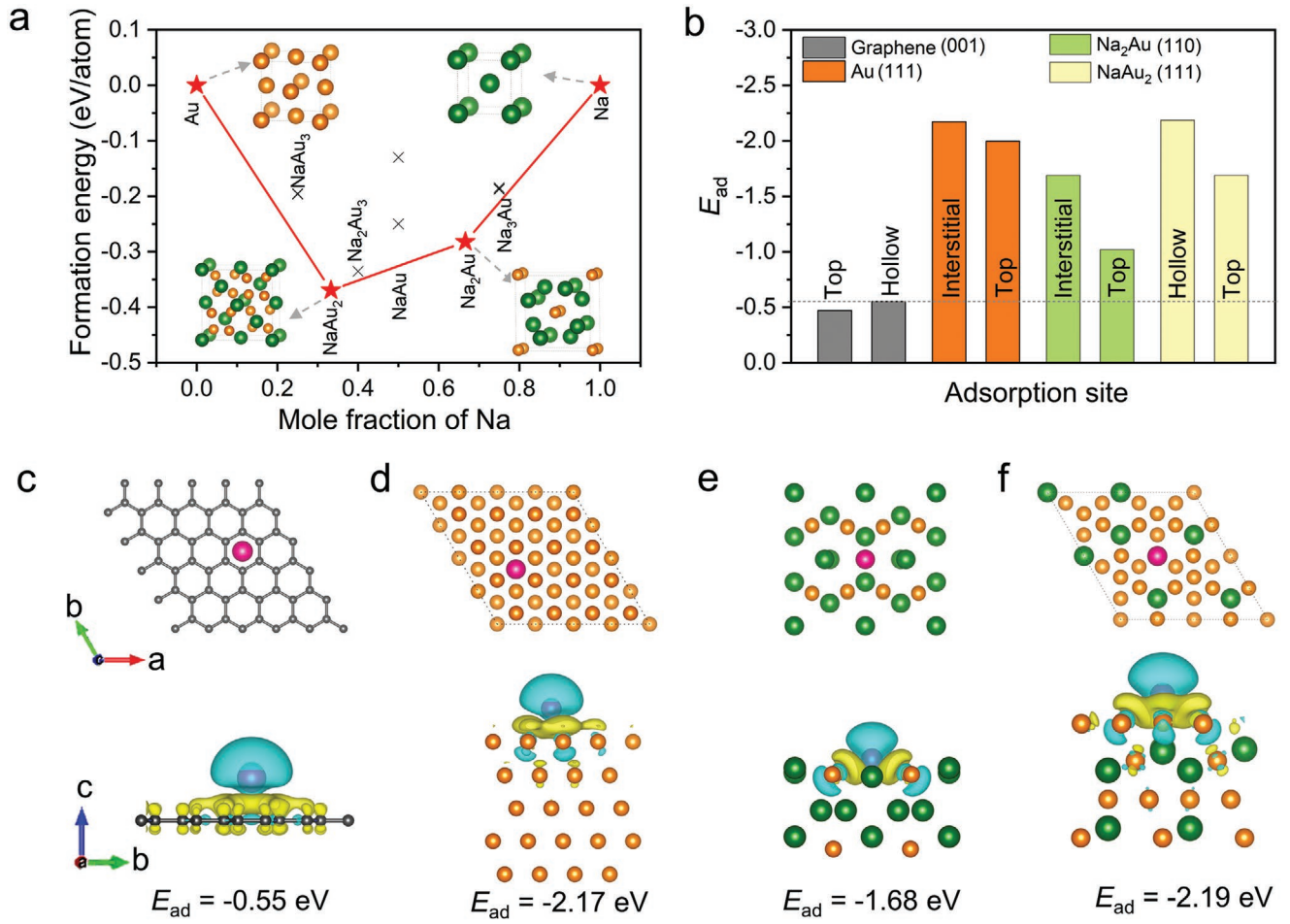

Figure 4. DFT calculations of Na affinity on different substrates. a) Formation energies of Na-Au binaries as a function of mole fraction of Na. b) Adsorption energies of an isolated Na atom on different substrates. Optimized structures and charge density difference plots of an isolated Na adsorbed on c) graphene (001), d) Au (111) plane, e) Na_2Au (110) plane, and f) $NaAu_2$ (111) plane. The pink, grey, orange, and green spheres represent adsorbed Na, C, Au, and Na atoms, respectively. The yellow and cyan surfaces in charge density difference plots correspond to the positive (charge gain) and negative (charge loss) regions, respectively.

and Na_2Au are thermodynamically stable alloys, in agreement with the previous reports.[34,35] Furthermore, the Na affinity with different substrates was estimated, and the adsorption energies, E_{ad} (see Section 4.4 for details), are reported in Figure 4b. The E_{ad} of an isolated Na atom on graphene was computed to be –0.55 eV, a value bigger than those on Au (–2.17 eV), $NaAu_2$ (–1.68 eV), and Na_2Au (–2.18 eV), indicating that Au and Au-Na alloys have higher sodiophilicity and are more favorable in adsorbing Na than carbon alone. The optimized structures and the corresponding charge density difference plots of an isolated Na adsorbed on four different substrates are shown in Figure 4c–f.

To investigate the Na-Au alloy interphases, we sputtered Au nanoparticles on Cu foil under the same condition. The cyclic voltammograms of the Na||Cu and Na||Au/Cu cells are shown in Figure S11a, Supporting Information. A pair of reduction and oxidation peaks close to 0 V were observed for both cells, in response to the Na plating and stripping processes. In the case of Na||Au/Cu battery, an extra oxidation peak appearing at ≈0.2 V is attributed to the dealloying process of Na_2Au to $NaAu_2$ upon anodic stripping, in agreement with the previous reports.[34,35] The XRD measurements were also conducted to confirm the formation of $NaAu_2$, as shown in Figure S11b, Supporting Information. For the pristine Au/Cu substrate, Au peaks were present. After the first sodiation/desodiation cycle, the $NaAu_2$ alloy was detected. The mass loadings of Au in Au/CF and Au/Cu were measured to be ≈0.04 mg cm^{-2}. Therefore, it can be said that the Na amount required for the alloying was less than 3 μAh cm^{-2}, which is negligible compared to the deposited amount.

2.3. Electrochemical Performance of the Au/CF Electrode

The effect of Au nuclei on electrochemical performance was evaluated in terms of CE, a measure of the plating/stripping reversibility, as shown in **Figure 5**a. Both the Au/CF and CF electrodes exhibited relatively high and stable CEs of ≈99.9% for 300 cycles at an areal current of 1 mA cm^{-2} and a low capacity of 1 mAh cm^{-2} for a plating time of 1 h (top panel of Figure 5a).

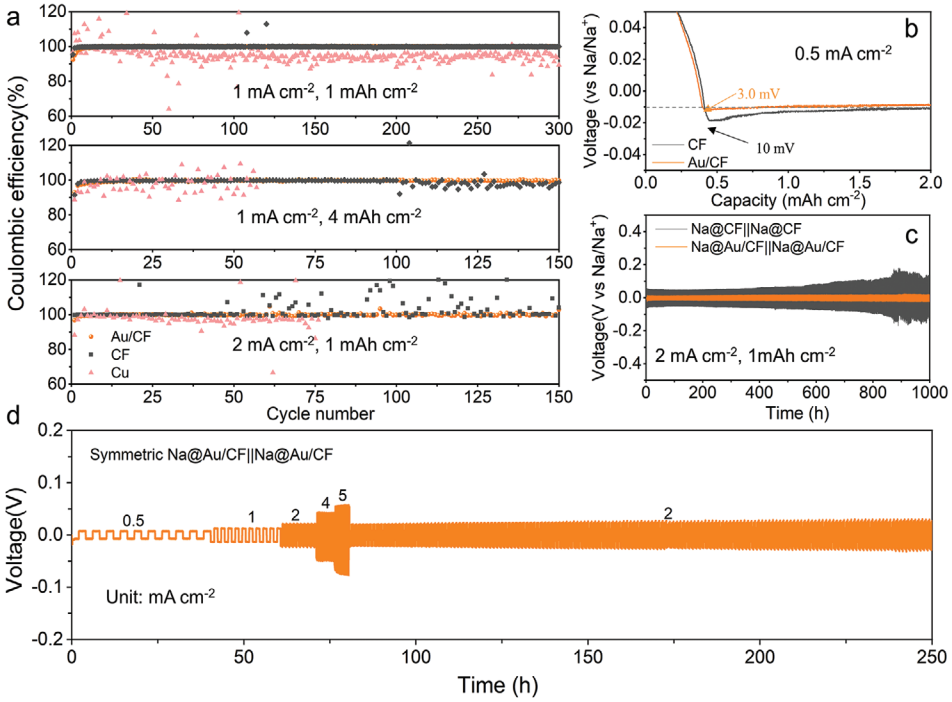

Figure 5. CE and symmetric cell performance of Au/CF host. a) CE versus cycle number plots of Au/CF, CF, and Cu measured at different areal currents and various deposition capacities. b) Electrochemical Na plating/stripping curves of the Au/CF and CF electrodes at 0.5 mA cm^{-2} with a specific capacity of 2 mAh cm^{-2}. c) Galvanostatic charge/discharge (GCD) voltage curves of the Na@Au/CF and Na@CF anodes in symmetrical cells at 2 mA cm^{-2} with a specific capacity of 1 mAh cm^{-2}. d) GCD curves of a symmetric Na@Au/CF cell at different areal currents and a specific capacity of 1 mAh cm^{-2}.

In contrast, the Cu foil displayed fluctuating CEs with an average CE lower than 95% after only 50 cycles, being associated with the growth and corrosion of Na dendrites. When the capacity was increased to 4 mAh cm^{-2}, the Au/CF electrode achieved a stable CE of ≈99.7% for 150 cycles. Instead, the CF material exhibited an irregular CE fluctuation after 50 cycles, a reflection of unstable deposition and dissolution of Na on CF (mid-panel of Figure 5a). Impressively, the Au/CF electrode maintained a high and stable CE of ≈99.7% for 1000 h, equivalent to 50 cycles, even when the plating capacity was increased to 10 mAh cm^{-2}, see Figure S12, Supporting Information. Also, it delivered a high average CE of 99.5% for 150 cycles when the areal current was 2 mA cm^{-2} (bottom panel of Figure 5a). In general, the overall CEs of the Au/CF electrode were far superior to the CF and Cu counterparts, a testament to the sodiophilic modification of the CF host with the Au coating which facilitated a "bottom-up growth" mode while avoiding the formation of Na dendrites on the top surface of substrates. The Au/CF exhibited an obvious lower overpotential of 35 mV than 57 mV obtained for CF at 2 mA cm^{-2}, demonstrating a beneficial effect of Au nuclei on electrode kinetics (Figure S13a, Supporting Information). In addition, the Au nanoparticles in the Au/CF host had a diameter of only ≈5 nm and were attached uniformly on in the porous carbon substrate, which effectively released the stress arising from sodiation. Therefore, the chance for Au pulverization would be negligible. As a result, during the repeated plating/stripping cycles, the Au/CF electrode maintained a stable overpotential of ≈35 mV and exhibited overlapping of voltage profiles that are representative of high reversibility, see FigureS13b, Supporting Information. It should be noted that the Au/CF host was much lighter, with an areal density of ≈1.5 mg cm^{-2}, than metal collectors (i.e., Cu or Ni) used in Na metal anodes. Therefore, the Na@Au/CF composite anode has a high specific gravimetric capacity. For example, when the areal capacity of Na@Au/CF was 10 mAh cm^{-2}, the Au/CF enabled the specific capacity of Na@Au/CF to reach ≈990 mAh g^{-1}, a value approaching that of pure Na metal. This finding signifies an added benefit of using the highly porous Au/CF hosts compared to planar or 3D metals.

Figure 5b compares the nucleation voltages for Na deposition on Au/CF and CF. Due to the affinity between Na and Au, the Au/CF has an ultralow plating overpotential of 3.0 mV at a current density of 0.5 mA cm^{-2}. In contrast, CF had an overpotential of ≈10.0 mV. To identify interfacial stability before and after 100 cycles, the symmetric cell schematically shown in Figure S7b, Supporting Information, was also probed by electrochemical impedance spectroscopy (EIS). Figure S14a,b, Supporting Information, present the Nyquist curves, and an equivalent circuit model (Figure S14c, Supporting Information) was used to fit the EIS spectra. As displayed in Table S1, Supporting Information, the Na@Au/CF||Na@Au/CF cell maintained stable resistance of SEI (R_{SEI}) and charge transfer resistance (R_{ct}) for 100 plating/stripping cycles. In contrast, the R_{SEI} and R_{ct} of the Na@CF||Na@CF cell increased gradually with cycle numbers, indicating the repeated formation of SEI and the growth of Na dendrites or dead Na. The variation of the

R_{SEI} and R_{ct} with cycle numbers in both symmetric cells was shown in Figure S14d, Supporting Information. The EIS results clearly illustrate the improved interfacial stability and favorable Na plating/stripping kinetics that are enabled for Au/CF host.

The cyclic stability of the two symmetric cells is shown in Figure 5c. The overpotential of the Na@Au/CF||Na@Au/CF cell was ≈20 mV at 2 mA cm^{-2} and kept constant for 1000 h of cycles, implying a stable Na plating/stripping behavior. In contrast, the overpotential of the Na@CF||Na@CF cell gradually increased to 120 mV after 800 h, consistent with the R_{ct} evolution. Moreover, the voltage profiles of the Na@Au/CF||Na@Au/CF symmetric cell displayed stable overpotential even at a high current density of 5 mA cm^{-2}. The overpotentials were 7, 12, 20, 41, and 52 mV, respectively, at areal currents of 0.5, 1, 2, 4, and 5 mA cm^{-2}, implying excellent rate capability of the Au/CF electrode (Figure 5d and Figure S15, Supporting Information). The cycle life and voltage hysteresis of the Na@Au/CF anodes are compared with the state-of-the-art Na metal anodes, see Table S2, Supporting Information, where it can be seen that the electrochemical performance of the current composite anode is among the best. The stable cycle life and low polarization potential of the Na@Au/CF||Na@Au/CF cell corroborate fast kinetics of Na^+ migration and superior interface properties, signifying the potential of employing the Na@Au/CF electrode for high-energy NMBs.

In light of the outstanding electrochemical properties of the Na@Au/CF composite anodes, full cells were assembled with NVPF and SPAN cathodes for demonstrating their practical applications. It should be noted that the reversible capacities for full cells are nominated for the mass of cathode materials. The corresponding cell configuration is shown in Figure S7c, Supporting Information, and the details regarding the NVPF and SPAN electrode preparation are given in the Experimental section.[5,43] Figure S16, Supporting Information, shows the XRD pattern, SEM image, and EDX elemental maps of NVPF. The long-term cyclic performance of the Na@Au/CF||NVPF full cell was investigated at 2 C, as shown in **Figure 6**a. The Na@Au/CF||NVPF cell delivered a capacity of 102.1 mAh g^{-1} after 500 cycles along with capacity retention of ≈91%, exhibiting impressive long-term durability. In contrast, the capacity of the Na@CF||NVPF cell was 89.2 mAh g^{-1} under the same testing condition, with a poorer capacity retention of ≈84%. For comparative studies, 2D Cu foil was also deposited with 4 mAh cm^{-2} Na to assemble Na/Cu||NVPF full cells. The battery showed a much faster capacity decay with a lower capacity of 78.4 mAh cm^{-2} after only 120 cycles than the Na@CF||NVPF cell, accompanied by fluctuating CEs. Furthermore, cyclic performance at 5 C was examined and compared with a high NVPF loading of 3 mg cm^{-2} (Figure 6b). As expected, the Na@Au/CF||NVPF cell presented the best performance with negligible capacity decay for 100 cycles, whereas the Na@CF||NVPF and Na/Cu||NVPF cells operated steadily only for 70 and 22 cycles, respectively.

Besides, the GCD profiles and rate performance of the Na@Au/CF||NVPF full cell were measured at different C rates (1 C = 120 mA g^{-1}), as shown in Figure 6c,d. Its discharge specific capacities were 111.4, 110, 109.2, 107.7, 104.3, and 88.6 mAh g^{-1} as the current density was increased from 0.5 to 15 C. In comparison, the Na@CF||NVPF and Na/Cu||NVPF cells maintained generally lower discharge capacities, notably of 63.7 and 48.6 mAh g^{-1} at 15 C, respectively. Meanwhile, when the NVPF mass loading was increased from 2.5 to 5 mg cm^{-2}, the Na@Au/CF||NVPF battery displayed much the same excellent cyclic stability for 100 cycles, see Figure 6e and Figure S17, Supporting Information. In addition to the NVPF cathode, Na@Au/CF||SPAN full cells were also assembled. The SEM images and EDX elemental maps of SPAN are shown in Figure S15, Supporting Information, while the GDC profiles of the Na@Au/CF||SPAN and Na@CF||SPAN full cells are displayed in Figure S19, Supporting Information. The Na@Au/CF||SPAN full cell delivered a high initial charge capacity of 906.4 mAh g^{-1} and maintained a high capacity of 650 mAh g^{-1} after 150 cycles at 0.5 C (1 C = 1670 mA g^{-1}) accompanied with a capacity decay of 0.38% per cycle. The corresponding values were generally lower for the Na@CF||SPAN full cell with a remaining discharge capacity of 300 mAh g^{-1} after 150 cycles at 0.5 C (Figure 6f), less than half that of Na@Au/CF||SPAN. Low-cost metals, such as Sn, Sb, and Zn, have been identified as potential alternatives to expensive Au for constructing sodiophilicity gradient hosts for Na metal anodes.

Finally, as a proof of concept, anode-free full cells consisting of Au/CF, CF, or Cu foil as anode and NVPF cathode were assembled. The substrates were cycled between 0 and 1V (vs Na/Na^+) at 0.1 mA cm^{-2} for the first five cycles to reduce the surface contamination. The Au/CF||NVPF cell delivered a reversible capacity of 67 mAh g^{-1} after 40 cycles, exhibiting much better cyclic performance than the CF||NVPF and Cu||NVPF cells, as shown in Figure S20, Supporting Information. Although the cyclic stability of these anode-free full cells was not excellent, we think it could be further improved using new electrolytes. For example, it was reported that fluorinated ether is compatible with both Li metal anodes and high-voltage cathodes with stable SEI.[44] Therefore, it is promising to develop new electrolytes that are stable against both Na metal anodes and high-voltage cathodes for high-energy Na batteries.

3. Conclusions

Herein, we report the development of novel Au/CF hosts for stable, high-energy-density NMBs using CF hosts coated with Au particles with a concentration gradient through its thickness. Au nanoparticles served as the sodiophilic nucleation sites, which in turn facilitated preferential Na plating from the Au-rich bottom surface toward the Au-deficient top surface of the 3D Au/CF electrode. Therefore, uniform deposition of Na was achieved through the entire Au/CF host thickness in the "bottom-up growth" mode. In addition, the novel strategy we explored in this study effectively eliminated the negative effect of the sodiophobic host on the energy density of the whole Na metal anode. As such, the Na@Au/CF anode presented stable Na plating/stripping behavior, high average CEs of ≈99.9%, and ultralong lifespan for over 1000 h. When the Na@Au/CF anode was paired with an NVPF cathode, the full cell delivered a fulfilling specific capacity of 102.1 mAh g^{-1} after 500 cycles at 2 C, accompanied by capacity retention of ≈91%. Further, the Na@Au/CF composite anode presented consistently better electrochemical performance than the Na@CF and Na/Cu counterparts when they were paired with two different cathode

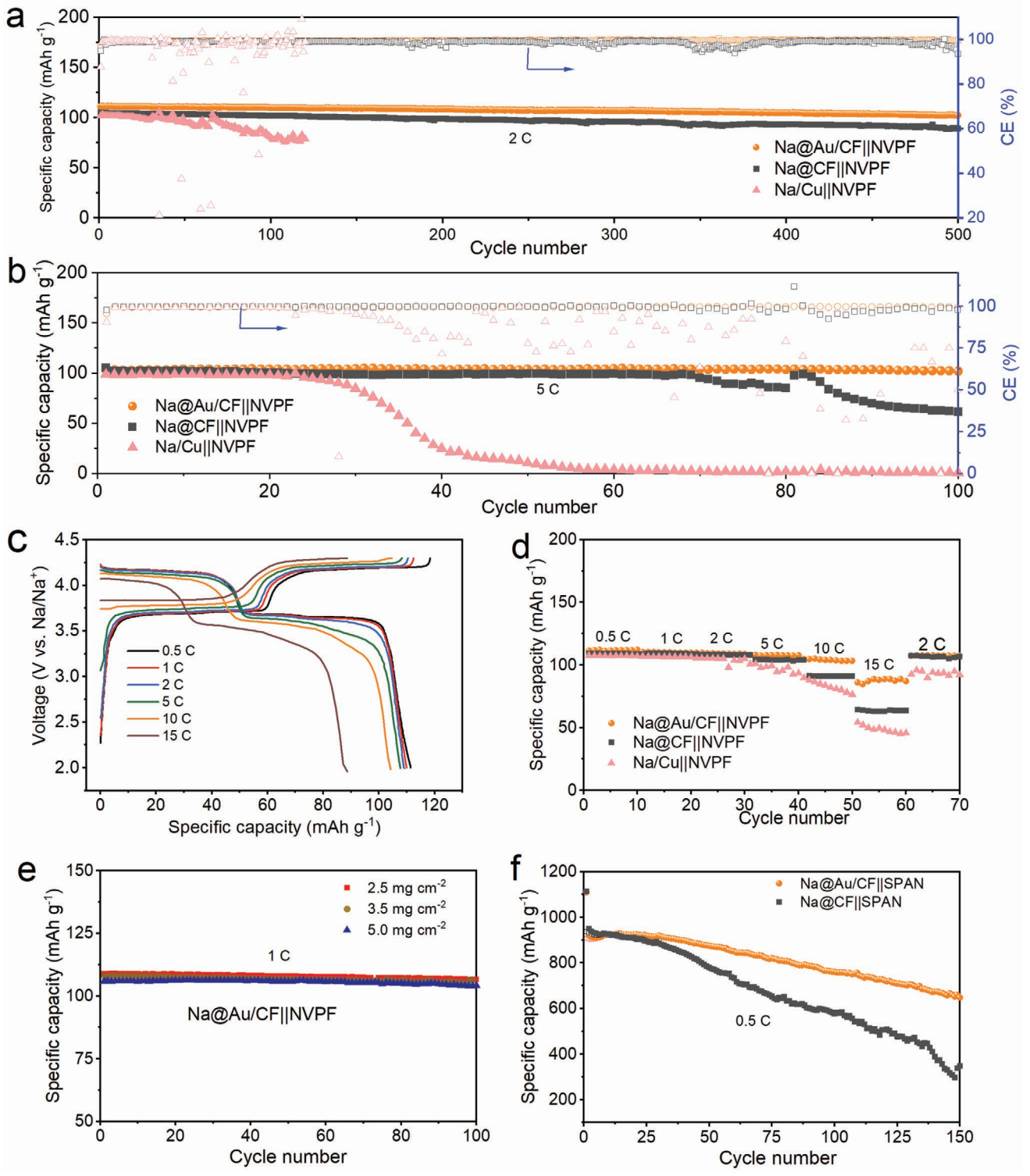

Figure 6. Electrochemical performance of the Na@Au/CF||NVPF, Na@CF||SPAN, and Na/Cu||NVPF full cells. Cyclic performance at a) 2 C and b) 5 C. c) Charge/discharge voltage profiles of the Na@Au/CF||NVPF full cell at different current densities. d) Rate capabilities of different full cells. e) Cyclic performance of Na@Au/CF||NVPF with different NVPF loadings at 1 C. f) Cyclic performance of the Na@Au/CF|| SPAN and Na@CF||SPAN cells at 0.5 C.

materials, NVPF and SPAN, for full cells, especially when measured at high C rates. The result of the full cell prepared using a high mass loading of NVPF electrode also remained highly consistent with the low mass loading counterpart, signifying potential real-world application of the electrode for NMBs with high energy densities.

4. Experimental Section

Fabrication of CF and Au/CF Electrode: A commercial melamine foam was washed with deionized water and ethanol to remove the surface impurities and dried for further use. Freestanding CF was obtained after carbonization of the cleaned melamine foam at 1000 °C for 2 h at a ramping rate of 2 °C min^{-1} under N_2 flow. Finally, the Au/CF host was obtained by sputtering Au nanoparticles on one side of the CF on a magnetron sputtering system (Denton Vacuum Discovery-18) at a sputtering power of 60 W for 45 s with Au in an Ar atmosphere at 5 m Torr. Similarly, Au/Cu substrate was prepared by replacing CF with Cu foil under the same conduction.

Materials Characterization: The microscopic morphology and elemental maps of Au/CF and CF were characterized by SEM (FE-SEM, JSM-7100). To examine the morphological changes of the aforementioned hosts after Na deposition, the disassembled samples were washed with DME and dried in an Ar-filled glove box (Mbraun). The cut pieces were stored in an Ar-filled box to transport to the SEM chamber. The HRTEM images and the corresponding SAED patterns were acquired on a JEOL-2010 microscope. In situ optical images were examined to visualize the Na plating/stripping behavior of the Au/CF and CF hosts. The XRD patterns were obtained on a Philips PW1830 diffractometer with Cu Kα radiation. The XPS spectra were recorded using an ESCALAB 250Xi (Thermo Fisher) with a monochromatic Al Ka source.

Electrochemical Measurements: To evaluate the CEs, CR2032-type coin cells were assembled using Au/CF, CF, and planar Cu as the working electrodes (ϕ12 mm) and Na foil (ϕ12 mm) as the counter/reference electrodes within an Ar-filled glove box. Celgard 2400 membrane was used as the separator, and 1 M $NaCF_3SO_3$ in diglyme (50 µL) was chosen as the electrolyte unless noted otherwise. The cells were cycled between 0 and 1 V (vs Na/Na^+) at 0.1 mA cm^{-2} for the first five cycles to reduce the surface contamination. Then a given amount of Na metal was deposited on the collectors/hosts at different areal currents and recharged to 1 V to strip the predeposited Na at the same current. The CE is defined as the ratio of stripped capacity to plated capacity. For testing of symmetric cells, the Au/CF and CF electrodes predeposited with 4 mAh cm^{-2} Na were assembled as both the working and counter/reference electrodes. The GCD tests were conducted on a LAND CT 2001A battery testing system, while the CV and EIS measurements were performed on a VSP electrochemical workstation (Biologic).

Full cells were assembled to evaluate the feasibility of the Na@Au/CF anode for real-world applications. The NVPF cathode was prepared by mixing NVPF, carbon black, and polyvinylidene difluoride at a weight ratio of 8:1:1 in *N*-methyl-2-pyrrolidone to form a homogeneous slurry. The slurry was coated onto aluminum foil, which was dried in a vacuum oven at 80 °C for 12 h. The active mass loading of NVPF cathodes ranged from 1.5 to 5 mg cm^{-2}. Similarly, the SPAN cathode was composed of 80 wt% SPAN, 10 wt% Super P, and 10 wt% sodium carboxymethyl cellulose binder. The mass loading of the SPAN cathode was 2–2.5 mg cm^{-2}. Both the NVPF and SPAN electrodes were punched into circular discs of 12 mm in diameter. The Au/CF and CF hosts were predeposited with 4 mAh cm^{-2} Na at an areal current of 0.5 mA cm^{-2}. 50 µL 1 M $NaClO_4$ in propylene carbonate (PC) containing 5 vol% fluoroethylene carbonate was used as the electrolyte, and the separator was prepared from glass microfibers (Whatman, GF/D). The Na@Au/CF||NVPF full cells were tested in a voltage window between 2.5 and 4.2 V while the Na@Au/CF||SPAN full cells were tested between 0.8 and 3 V. Finally, anode-free full cells consisting of NVPF cathode and Au/CF, CF, or Cu foil were assembled. The mass loading of NVPF is ≈6 mg cm^{-2}.

Theoretical Calculations: All spin-polarized DFT calculations were performed under the general gradient approximation using the Perdew–Burke–Ernzerhof functionals as implemented in the Vienna ab initio simulation package.[45–48] The core-electrons were treated with the projector augmented wave method. The kinetic cutoff for plane-waves was set at 450 eV. The structures of graphene, Au, $NaAu_2$, and Na_2Au were first optimized. The bottom two of five layers of (2 × 2) supercell of Au (111), Au_2Na (111), and $AuNa_2$ (111) slabs were fixed, and a vacuum layer of 15 Å was set along the *z*-axis in the supercell. 6 × 6 × 1 Γ-centered k-point sampling grid was used for geometric optimization. For each structural relaxation, both the ion positions and the lattice parameters were allowed to change until the Hellman–Feynman force on each ion dropped below 0.01 eV $Å^{-1}$. The adsorption energies, E_{ad}, of an isolated Na atom on the surface of different slabs were calculated using the following equation:

$$E_{ad} = E_{slab+Na} - E_{slab} - E_{Na} \quad (1)$$

where $E_{slab+Na}$ is the energy of one Na atom adsorbed on the surface of graphene, Au, $AuNa_2$, or Au_2Na; E_{slab} is the energy of a specific slab, and E_{Na} is the energy of Na atom in a sodium crystal.

Supporting Information

Supporting Information is available from the Wiley Online Library or from the author.

Acknowledgements

This project was financially supported by the Research Grants Council (GRF Projects: 16207615, 16227016, 16204517, and 16208718) and the Innovation and Technology Commission (ITS/292/18FP) of Hong Kong SAR. The authors also acknowledge the support from the Guangzhou Science and Technology Program (No. 201807010074). The authors also appreciate the technical assistance from the Advanced Engineering Materials Facilities (AEMF) and the Materials Characterization and Preparation Facilities (MCPF) of HKUST.

Conflict of Interest

The authors declare no conflict of interest.

Keywords

Au coating, carbon foam, sodiophilicity gradients, sodium metal

Received: June 23, 2020
Revised: August 10, 2020
Published online: September 2, 2020

[1] D. Lin, Y. Liu, Y. Cui, *Nat. Nanotechnol.* **2017**, *12*, 194.
[2] X.-B. Cheng, R. Zhang, C.-Z. Zhao, Q. Zhang, *Chem. Rev.* **2017**, *117*, 10403.
[3] J. Xiang, L. Yang, L. Yuan, K. Yuan, Y. Zhang, Y. Huang, J. Lin, F. Pan, Y. Huang, *Joule* **2019**, *3*, 2334.
[4] L. Ma, J. Cui, S. Yao, X. Liu, Y. Luo, X. Shen, J.-K. Kim, *Energy Storage Mater.* **2019**, *27*, 522.
[5] J. Wu, J. Liu, Z. Lu, K. Lin, Y.-Q. Lyu, B. Li, F. Ciucci, J.-K. Kim, *Energy Storage Mater.* **2019**, *23*, 8.
[6] B. Lee, E. Paek, D. Mitlin, S.-W. Lee, *Chem. Rev.* **2019**, *119*, 5416.
[7] X. Zheng, C. Bommier, W. Luo, L. Jiang, Y. Hao, Y. Huang, *Energy Storage Mater.* **2019**, *16*, 6.
[8] J. Cui, S. Yao, M. Ihsan-Ul-Haq, J. Wu, J.-K. Kim, *Adv. Energy Mater.* **2019**, *9*, 1802777.
[9] Y. Zhao, K. R. Adair, X. Sun, *Energy Environ. Sci.* **2018**, *11*, 2673.
[10] B. Sun, P. Li, J. Zhang, D. Wang, P. Munroe, C. Wang, P. H. L. Notten, G. Wang, *Adv. Mater.* **2018**, *30*, 1801334.
[11] Z. W. Seh, J. Sun, Y. Sun, Y. Cui, *ACS Cent. Sci.* **2015**, *1*, 449.

[12] J. Lee, Y. Lee, J. Lee, S.-M. Lee, J.-H. Choi, H. Kim, M.-S. Kwon, K. Kang, K. T. Lee, N.-S. Choi, *ACS Appl. Mater. Interfaces* **2017**, *9*, 3723.
[13] S. Wang, Y. Chen, Y. Jie, S. Lang, J. Song, Z. Lei, S. Wang, X. Ren, D. Wang, X. Li, *Small Methods* **2020**, *4*, 1900856.
[14] W. Luo, C. F. Lin, O. Zhao, M. Noked, Y. Zhang, G. W. Rubloff, L. Hu, *Adv. Energy Mater.* **2017**, *7*, 1601526.
[15] Y. Zhao, L. V. Goncharova, Q. Zhang, P. Kaghazchi, Q. Sun, A. Lushington, B. Wang, R. Li, X. Sun, *Nano Lett.* **2017**, *17*, 5653.
[16] S. Choudhury, S. Wei, Y. Ozhabes, D. Gunceler, M. J. Zachman, Z. Tu, J. H. Shin, P. Nath, A. Agrawal, L. F. Kourkoutis, T. A. Arias, L. A. Archer, *Nat. Commun.* **2017**, *8*, 898.
[17] C. Wang, H. Wang, E. Matios, X. Hu, W. Li, *Adv. Funct. Mater.* **2018**, *28*, 1802282.
[18] S.-S. Chi, X.-G. Qi, Y.-S. Hu, L.-Z. Fan, *Adv. Energy Mater.* **2018**, *8*, 1702764.
[19] Y. Zhao, X. Yang, L. Y. Kuo, P. Kaghazchi, Q. Sun, J. Liang, B. Wang, A. Lushington, R. Li, H. Zhang, *Small* **2018**, *14*, 1703717.
[20] S. Liu, S. Tang, X. Zhang, A. Wang, Q.-H. Yang, J. Luo, *Nano Lett.* **2017**, *17*, 5862.
[21] A. Wang, X. Hu, H. Tang, C. Zhang, S. Liu, Y. W. Yang, Q. H. Yang, J. Luo, *Angew. Chem., Int. Ed.* **2017**, *129*, 12083.
[22] W. Luo, Y. Zhang, S. Xu, J. Dai, E. Hitz, Y. Li, C. Yang, C. Chen, B. Liu, L. Hu, *Nano Lett.* **2017**, *17*, 3792.
[23] C. Chu, N. Wang, L. Li, L. Lin, F. Tian, Y. Li, J. Yang, S.-X. Dou, Y. Qian, *Energy Storage Mater.* **2019**, *23*, 137.
[24] N. Mubarak, M. Ihsan-Ul-Haq, H. Huang, J. Cui, S. Yao, A. Susca, J. Wu, M. Wang, X. Zhang, B. Huang, J.-K. Kim, *J. Mater. Chem. A* **2020**, *8*, 10269.
[25] J. L. Ma, Y. B. Yin, T. Liu, X. B. Zhang, J. M. Yan, Q. Jiang, *Adv. Funct. Mater.* **2018**, *28*, 1703931.
[26] X. Yu, L. Xue, J. B. Goodenough, A. Manthiram, *ACS Mater. Lett.* **2019**, *1*, 132.
[27] Y.-Q. Lyu, J. Yu, J. Wu, M. B. Effat, F. Ciucci, *J. Power Sources* **2019**, *416*, 21.
[28] T.-S. Wang, Y. Liu, Y.-X. Lu, Y.-S. Hu, L.-Z. Fan, *Energy Storage Mater.* **2018**, *15*, 274.
[29] J. Luo, C. Wang, H. Wang, X. Hu, E. Matios, X. Lu, W. Zhang, X. Tao, W. Li, *Adv. Funct. Mater.* **2019**, *29*, 1805946.
[30] Z. Zheng, X. Zeng, H. Ye, F. Cao, Z. Wang, *ACS Appl. Mater. Interfaces* **2018**, *10*, 30417.
[31] M. Zhu, S. Li, B. Li, Y. Gong, Z. Du, S. Yang, *Sci. Adv.* **2019**, *5*, eaau6264.
[32] M. E. Lee, S. Lee, J. Choi, H. J. Jin, S. Han, Y. S. Yun, *Small* **2019**, *15*, 1901274.
[33] Z. Wang, X. Zhang, S. Zhou, K. Edström, M. Strømme, L. Nyholm, *Adv. Funct. Mater.* **2018**, *28*, 1804038.
[34] S. Tang, Z. Qiu, X.-Y. Wang, Y. Gu, X.-G. Zhang, W.-W. Wang, J.-W. Yan, M.-S. Zheng, Q.-F. Dong, B.-W. Mao, *Nano Energy* **2018**, *48*, 101.
[35] S. Tang, Y.-Y. Zhang, X.-G. Zhang, J.-T. Li, X.-Y. Wang, J.-W. Yan, D.-Y. Wu, M.-S. Zheng, Q.-F. Dong, B.-W. Mao, *Adv. Mater.* **2019**, *31*, 1807495.
[36] W.-S. Xiong, Y. Jiang, Y. Xia, Y. Qi, W. Sun, D. He, Y. Liu, X.-Z. Zhao, *Chem. Commun.* **2018**, *54*, 9406.
[37] Y. Zhang, C. Wang, G. Pastel, Y. Kuang, H. Xie, Y. Li, B. Liu, W. Luo, C. Chen, L. Hu, *Adv. Energy Mater.* **2018**, *8*, 1800635.
[38] L. Ye, M. Liao, T. Zhao, H. Sun, Y. Zhao, X. Sun, B. Wang, H. Peng, *Angew. Chem., Int. Ed.* **2019**, *131*, 17210.
[39] J. Pu, J. Li, K. Zhang, T. Zhang, C. Li, H. Ma, J. Zhu, P. V. Braun, J. Lu, H. Zhang, *Nat. Commun.* **2019**, *10*, 1.
[40] H. Zhang, X. Liao, Y. Guan, Y. Xiang, M. Li, W. Zhang, X. Zhu, H. Ming, L. Lu, J. Qiu, *Nat. Commun.* **2018**, *9*, 1.
[41] B. Hong, H. Fan, X.-B. Cheng, X. Yan, S. Hong, Q. Dong, C. Gao, Z. Zhang, Y. Lai, Q. Zhang, *Energy Storage Mater.* **2019**, *16*, 259.
[42] J. Xiang, L. Yuan, Y. Shen, Z. Cheng, K. Yuan, Z. Guo, Y. Zhang, X. Chen, Y. Huang, *Adv. Energy Mater.* **2018**, *8*, 1802352.
[43] M. Ihsan-Ul-Haq, H. Huang, J. Wu, J. Cui, S. Yao, W. G. Chong, B. Huang, J.-K. Kim, *Nano Energy* **2020**, *71*, 104613.
[44] C. V. Amanchukwu, Z. Yu, X. Kong, J. Qin, Y. Cui, Z. Bao, *J. Am. Chem. Soc.* **2020**, *142*, 7393.
[45] J. Wu, Z. Lu, K. Li, J. Cui, S. Yao, M. Ihsan-Ul Haq, B. Li, Q.-H. Yang, F. Kang, F. Ciucci, J.-K. Kim, *J. Mater. Chem. A* **2018**, *6*, 5668.
[46] J. Wu, J. Liu, J. Cui, S. Yao, M. Ihsan-Ul-Haq, N. Mubarak, E. Quattrocchi, F. Ciucci, J.-K. Kim, *J. Mater. Chem. A* **2020**, *8*, 2114.
[47] G. Kresse, J. Furthmüller, *Phys. Rev. B* **1996**, *54*, 11169.
[48] J. P. Perdew, K. Burke, M. Ernzerhof, *Phys. Rev. Lett.* **1996**, *77*, 3865.